

LINE-DRIVEN DISK WINDS IN ACTIVE GALACTIC NUCLEI: THE CRITICAL IMPORTANCE OF IONIZATION AND RADIATIVE TRANSFER

NICK HIGGINBOTTOM

School of Physics and Astronomy, University of Southampton, Highfield, Southampton, SO17 1BJ, UK

DANIEL PROGA

Department of Physics & Astronomy, University of Nevada, Las Vegas, 4505 S. Maryland Pkwy, Las Vegas, NV 89154-4002, USA

CHRISTIAN KNIGGE

School of Physics and Astronomy, University of Southampton, Highfield, Southampton, SO17 1BJ, UK

KNOX S. LONG

Space Telescope Science Institute, 3700 San Martin Drive, Baltimore, MD 21218, USA

JAMES H. MATTHEWS

School of Physics and Astronomy, University of Southampton, Highfield, Southampton, SO17 1BJ, UK

AND

STUART A. SIM

School of Mathematics and Physics, Queens University Belfast, University Road, Belfast, BT7 1NN, Northern Ireland, UK

Draft version July 18, 2018

ABSTRACT

Accretion disk winds are thought to produce many of the characteristic features seen in the spectra of active galactic nuclei (AGN) and quasi-stellar objects (QSOs). These outflows also represent a natural form of feedback between the central supermassive black hole and its host galaxy. The mechanism for driving this mass loss remains unknown, although radiation pressure mediated by spectral lines is a leading candidate. Here, we calculate the ionization state of, and emergent spectra for, the hydrodynamic simulation of a line-driven disk wind previously presented by Proga & Kallman (2004). To achieve this, we carry out a comprehensive Monte Carlo simulation of the radiative transfer through, and energy exchange within, the predicted outflow. We find that the wind is much more ionized than originally estimated. This is in part because it is much more difficult to shield any wind regions effectively when the outflow itself is allowed to reprocess and redirect ionizing photons. As a result, the calculated spectrum that would be observed from this particular outflow solution would not contain the ultraviolet spectral lines that are observed in many AGN/QSOs. Furthermore, the wind is so highly ionized that line-driving would not actually be efficient. This does not necessarily mean that line-driven winds are not viable. However, our work does illustrate that in order to arrive at a self-consistent model of line-driven disk winds in AGN/QSO, it will be critical to include a more detailed treatment of radiative transfer and ionization in the next generation of hydrodynamic simulations.

Subject headings: accretion, accretion disks - galaxies: active - methods: numerical - quasars: general - radiative transfer

1. INTRODUCTION

Outflows are found in a vast range of accreting astrophysical objects, from protostars to active galactic nuclei (AGN). In all of these settings, quantifying the mass and energy flows involved is key to understanding how the accreting objects evolve and interact with their local environment. In the case of AGN, the observed outflows can be split into two main classes: highly collimated, relativistic jets, and slower moving ($v \lesssim 0.2c$), but more massive ‘disk winds’ driven from the surface of the accretion disk surrounding the central supermassive black hole. These disk winds have been proposed as the underlying structure responsible for many observed AGN spectral features, including the broad absorption lines seen in a significant proportion of QSOs (e.g. Knigge et al.

2008), the so called broad absorption line quasars (BALQSOs). However, the geometry of these winds, and even the mechanism by which they are launched, are still not known.

Several mechanisms have been proposed to produce the accelerating force for disk winds in AGN, including gas/thermal pressure (e.g. Weymann et al. 1982; Begelman, De Kool & Sikora 1991; Begelman, McKee & Shields 1983; Krolik & Kriss 2001), magnetocentrifugal forces (e.g. Blandford & Payne 1982; Pelletier & Pudritz 1992) and radiation pressure acting on spectral lines (“line-driving”) (e.g. Shlosman, Vitello & Shaviv 1985; Murray et al. 1995). All of these mechanisms have been shown to produce outflows in suitable conditions. However, line driving is particularly attractive, since the requisite force in this case arises naturally when (primarily ultraviolet [UV]) photons produced

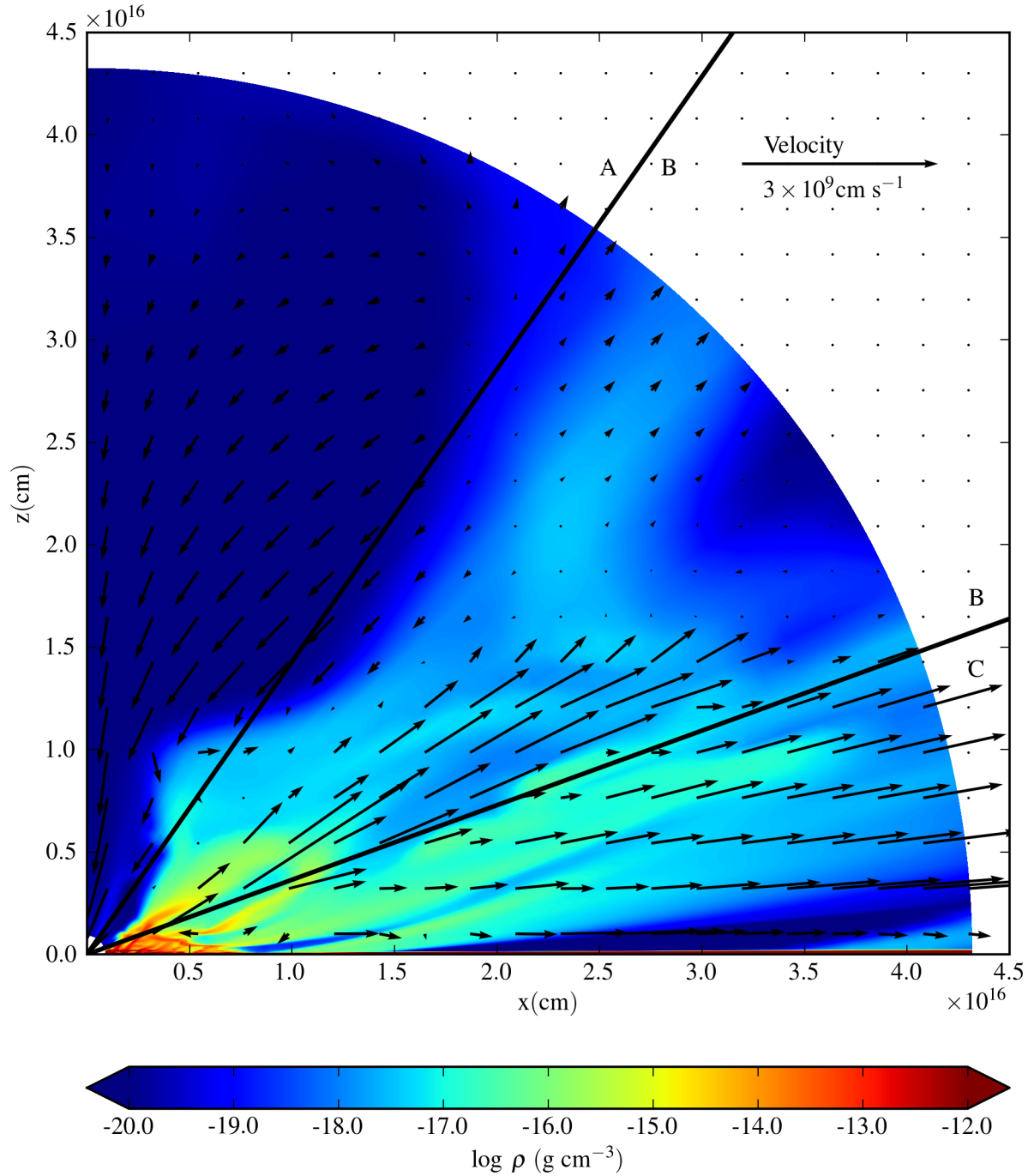


Figure 1. The density (colours) and poloidal velocity (arrows) structure of the PK04 model. Radial lines delineate the three zones described in the text.

by the central engine are scattered by strong resonance lines. Many such lines are observed directly in the UV spectra of (BAL)QSOs, so line driving must certainly be acting in some measure. Moreover, if line driving is the dominant acceleration mechanism, it can produce a unique signature in the profiles of absorption lines produced in the wind (the so-called “ghost of Ly α ”, e.g. Arav et al. 1995; Arav 1996), and this may already have been seen in several BALQSOs (North, Knigge & Goad 2006, but also see Cottis et al. 2010).

Despite these circumstantial reasons for favouring line-

driving as the mechanism for the production of disk winds in AGN, there is one main challenge to the model. For line-driving to be efficient, the accelerated material has to be in a moderately low ionization state, despite its proximity to the intense X-ray source at the center of the accretion disk. If the gas becomes over-ionized, the ionic species that can most effectively tap into the momentum of the radiation field are simply not present.

Murray et al. (1995) proposed one solution, suggesting that ‘hitchhiking gas’, material interior to the main out-

flow and itself accelerated by pressure differences can shield the line-driven wind from the central X-rays. Simulations such as those presented in Proga, Stone & Kallman (2000) and Proga & Kallman (2004, hereafter PK04) also produce a shield, but in this case via a ‘failed wind’. This failed wind arises close to the X-ray-emitting region and quickly becomes over-ionized as it rises above the disk surface. As it falls back, it produces a dense shield that prevents the intense X-ray radiation from reaching the outer parts of the outflow in its shadow. These low-ionization regions are then able to interact with UV radiation and give rise to a strong line-driven wind. The same type of shielding structure has also been seen in other models of disk winds (e.g. Risaliti & Elvis 2010; Nomura et al. 2013).

PK04 used hydrodynamical simulations to investigate whether a line-driven outflow could be accelerated to high velocities purely by the radiation field produced by the accretion disk. They estimated the ionization state and temperature of the wind, taking into account only the central source of ionizing radiation, attenuated by electron scattering. Their main result was that the ionization state of the wind behind the failed wind region remained low enough to permit line driving, so that a fast, dense outflow was generated. Absorption line profiles calculated from their wind model resembled those observed in BALQSOs (e.g. see Fig. 2 in Proga & Kurosawa 2010). It is worth noting that PK04’s wind, and especially its base, are virialized systems. This is because a line-driven wind accelerates slowly, so the rotational velocity is dominant over a relatively large distance while the wind base is Keplerian and very dense. This means that, if the broad line region (BLR) is associated with such a wind, black hole (BH) mass estimates based upon the assumption that the BLR is virialized remain correct (Kashi et al. 2013).

The PK04 wind model has already been subjected to two more detailed ‘post-processing’ radiative transfer calculations. Both of these were concerned with the impact of the predicted outflow on the X-ray spectra of AGN/QSO. First, Schurch, Done & Proga (2009) performed a 1-D simulation which found that the wind produced observable X-ray spectral features. Second, Sim et al. (2010, hereafter SP10) carried out a multi-dimensional radiative transfer simulation in which the ionization state and temperature structure of the wind were self-consistently computed. They confirmed that the wind was able to imprint a variety of characteristic features into the X-ray spectra of AGN. However, they also showed that scattering in the (failed) outflow is critically important in setting the ionization state of the wind in regions that would otherwise be shielded from the central engine.

PK04 used a simplified treatment of radiative transfer and ionization in their hydrodynamical simulations. These simplifications were essential to make the simulations computationally feasible. However, the work of SP10 implies that a careful treatment of radiative transfer may be required in order to obtain a reliable estimate of the ionization state of the wind. Since the ionization state, in turn, determines the efficiency of the line-driving mechanism itself, it is clearly important to check whether the wind model calculated by PK04 could actually maintain an ionization state that is consistent with efficient line driving and with the production of broad UV absorption lines.

Here, we therefore carry out a full, multi-dimensional radiative transfer calculation for the PK04 model that allows us to predict the ionization state, temperature structure and emergent UV spectra for this outflow. This extends the work done

by SP10 to the longer wavelengths and lower ionization stages that are critical to allow effective line-driving and the formation of BALs. In particular, we account for the low-energy (< 0.1 keV) photons that affect the abundances of key ions, such as C IV, N V and O VI. We also calculate emergent spectra throughout the UV band, where the BAL features associated with the resonance transitions of these species are found.

2. METHOD

In this section, we will introduce the radiative transfer code we use and review the geometry and kinematics of the outflow computed by PK04. We also describe the form of the illuminating spectrum we adopt and discuss how it relates to that used in PK04 and SP10.

2.1. PYTHON - a Monte Carlo radiative transfer and photoionization code

We use the hybrid Monte Carlo / Sobolev code PYTHON for our calculations. This was originally described in Long & Knigge (2002) and updated in Higginbottom et al. (2013). Briefly, our simulation tracks photon-packets produced from a geometrically thin accretion disk, modelled as a series of blackbodies, and a central source of radiation that can be used to simulate an X-ray emitting corona. These packets are tracked through the wind, and their heating and cooling effect is computed. The ionization state is calculated using a model of the mean intensity in each cell of the simulation, calculated from the photon packets that pass through it. Once a converged ionization state and temperature has been computed for the wind, synthetic spectra can be produced for any required sightline.

The heating and cooling rates in a given cell include contributions from free-free, bound-free, bound-bound and Compton processes. Dielectronic recombination is accounted for as a bound-free cooling term. The ionization state in the cell is calculated under the assumption that the dominant ionization process is photo-ionization from the ground state, which is balanced by radiative recombinations from the ground state to all levels, plus dielectronic recombinations. Convergence to the correct thermal and ionization equilibrium solutions is achieved by iteration, starting from an initial guess at the temperature and ionization state. In each iteration, or ‘ionization cycle’, a representative population of photon-packets is tracked as it makes its way through the wind. The energy deposited by these photons in each cell provides an estimate of the heating rate, so the temperature of the cell can be adjusted to yield a more closely matching cooling rate. The new temperature estimate is then used to obtain an updated estimate of the ionization state of the cell. These updated cell properties then form the basis for the next ionization cycle. The calculations presented here were carried out using version 77 of PYTHON and include H, He, C, N, O, Ne, Na, Mg, Al, Si, S, Ar, Ca and Fe.

2.2. The PK04 disk wind geometry

We take as our input the hydrodynamic wind model computed by PK04 at time-step 955. This represents a time sufficiently far from the simulation start that the wind geometry no longer depends on initial conditions. In addition, at this point, the flow is only weakly time-dependent, so this time-step is broadly representative of the flow as a whole. The figures in PK04 also focused on this time-step, as did both SP10 and Schurch, Done & Proga (2009). The hydrodynamic calculations in PK04 were carried out using ZEUS (Stone & Norman

1992), modified to include the effect of the radiation field on the driving force and the temperature balance of the wind. The model is illustrated in Figure 1, with the poloidal component of velocity field superimposed upon the density structure. PK04 noted three main regions (delineated on Figure 1 by radial lines):

- A: A hot, low-density, infalling region near the pole.
- B: A hot transition zone in which the wind struggles to escape.
- C: A warm, dense, equatorial flow that is shielded from the central source by a high-density ‘failed wind’ region close to the origin

The ZEUS grid is polar, logarithmic in both the r - and θ -direction, with finer discretisation close to the disk and the origin. To carry out the radiative transfer calculation, we create an identical grid and import the density and velocity structure of the ZEUS model. The density in each of our grid cells is constant and taken to be the value at the centre of each matching grid cell in the hydrodynamic model, whilst the velocity field in each cell is interpolated across each cell based upon the values at the vertices in the original model. This discretization of the velocity field lends itself more naturally to our use of the Sobolev approximation in the treatment of line scattering.

Figure 2 shows the same density information as Figure 1, but on logarithmic axes in order to highlight the dense parts of the wind closer to the disk plane. This shows a wedge-like region at the base of the wind - the disk atmosphere. In our code, photons emitted by the accretion disk start from the disk plane and therefore would have to make their way through this atmosphere before entering the rest of the wind. Such dense regions, in which photons scatter a very large number of times, are extremely computationally expensive in a Monte-Carlo code. We therefore remove this part of the flow from the computation, permitting photons to fly unimpeded from the disk into the lower part of the wind. This is a reasonable approximation since, to first order, the dense disk atmosphere would be expected to thermalise to the same temperature as the disk beneath it. Hence the upper surface of that region would be expected to emit photons with the same spectral distribution as our disk.

The black line in Figure 2 shows the angle at which we make this cut - $\theta = 89.5^\circ$. The temperature of the lower surface of the flow where it is primarily irradiated by photons from the disk is approximately equal to the disk below it. This is the same as would be expected if the surface was in direct contact with the upper surface of an extended disk atmosphere. We are therefore confident that this simplification does not significantly affect the results obtained for the bulk of the wind.

2.3. Illuminating spectrum

Given the density and velocity structure of the wind, we next need to specify the parameters of the radiation sources in our model, i.e. the accretion disk and X-ray-emitting central ‘corona’. To permit comparison between our results and those of PK04 and SP10, we match the parameters used in those studies as closely as possible.

PK04 assumed the presence of a $10^8 M_\odot$ supermassive BH at the centre of their accretion disk and adopted an accretion rate on the BH of $1.8 M_\odot \text{yr}^{-1}$. This gives a disk luminosity

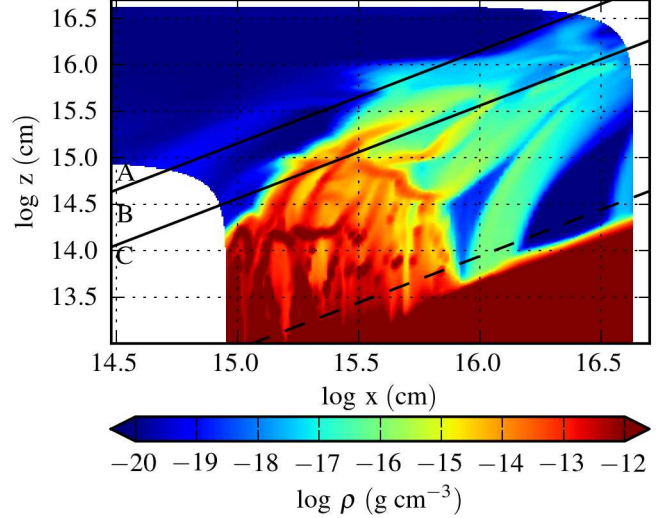


Figure 2. The density of the PK04 model, plotted on logarithmic axes. The solid lines show the boundaries between the three zones described in the text, and the dashed line at $\theta = 89.5^\circ$ is where we truncated the wind in our representation of the model.

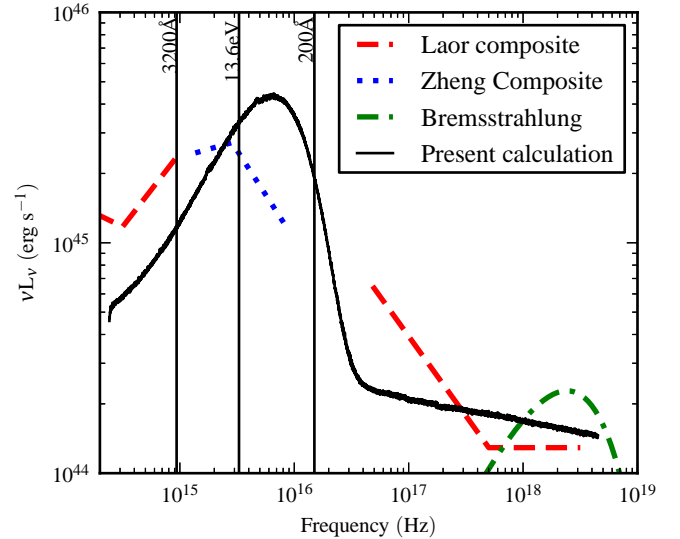


Figure 3. The input spectrum using the simulation, together with the 10 keV bremsstrahlung spectrum assumed in the original PK04 calculation. Also shown are the composite spectra from Laor et al. (1997) and Zheng et al. (1997) used to inform the luminosities used in PK04. The vertical lines illustrate the positions of various band boundaries discussed in the text

of $L_D = 6.1 \times 10^{45} \text{ ergs s}^{-1}$ assuming an efficiency of $\approx 6\%$. In their hydrodynamic simulation, PK04 split the illuminating luminosity into two components. First, they defined an ‘ionizing’ luminosity (L_X) that was used to compute the temperature and ionization parameter throughout the wind. Second, they defined a ‘UV’ luminosity (L_{UV}) that was used to compute the actual line-driving force. However, in regions of the wind that are shielded from the X-ray source by optically thick material, the wind temperature was set to that of the disk below the wind, thus implicitly assuming that these parts of the wind would be heated and ionized by disk photons.

The balance between the two components was motivated by the composite spectra presented in Laor et al. (1997) and

Zheng et al. (1997); the radio quiet composite is shown in Figure 3. The ‘ionizing luminosity’, L_X , defined by PK04 as the integrated luminosity of the central source above 13.6 eV (912 Å), was taken to be 10% of L_D , or 6.1×10^{44} ergs s^{-1} . The ionization parameter at any point in the flow was then computed from the local X-ray flux by assuming $1/r^2$ geometric dilution as well as $e^{-\tau_{es}}$ attenuation, where τ_{es} is the optical depth towards the origin due to electron scattering. This ionization was then used to calculate the line-driving force using the analytic formulae of Stevens & Kallman (1990). These formulae assume that the frequency distribution of ionizing photons takes the form of a 10 keV bremsstrahlung spectrum with no low-frequency cutoff. The calculations of the wind temperature structure in PK04 used the same characteristic temperature for the X-ray source in order to ensure self-consistency. A bremsstrahlung spectrum of this form, normalised to give the correct value of L_X is also plotted on Figure 3.

The UV luminosity in PK04 was defined as the luminosity in a band running from 200 to 3000 Å and was set to 90% of L_D . It should be noted that there is a degree of inconsistency here - a significant part of the ‘UV’ band is actually above the 13.6eV lower limit of the ‘ionizing’ band, and we see from Figure 3 that the composite spectrum carries significant ionizing luminosity that would contribute to L_X , as well as L_{UV} . However, increasing L_X to take account of this would mean that the luminosity around the peak of the bremsstrahlung spectrum would be much too high. This illustrates the difficulty of approximating an observed SED with a highly simplified model.

In our current calculation, we use a thin accretion disk with the same BH mass and accretion rate adopted by PK04, even though such a model may not produce the best match to observations (e.g Davis & Laor 2011; Done et al. 2012; Slone & Netzer 2012). We also include a power-law X-ray source assumed to arise in a central spherical ‘corona’. This X-ray source is defined by the same photon index, Γ , and luminosity in the 2–10 keV range, L_{2-10} , that was used by SP10. In that work, the X-ray parameters were chosen so as to give a reasonable match to observations whilst maintaining the same luminosity in the 2–10 keV range as the X-ray parameters in PK04. More specifically, we follow SP10 in adopting $L_{2-10} = 2.7 \times 10^{44}$ ergs s^{-1} and $\Gamma_X = 2.1$. Moreover, following PK04, we set the radius of the X-ray source, r_X , equal to the innermost radius of the accretion disk (which we take to be the innermost stable circular orbit, $R_{ISCO} = 6R_g$ for a Schwarzschild black hole, where R_g is the gravitational radius). With these choices, our SED yields $L_X \sim 0.7L_D$ and $L_{UV} \sim 0.9L_D$ in the notation of PK04. Note the two components sum to more than unity because we count ionizing photons from the disk in both L_X and L_{UV} . Figure 3 shows that our SED provides a reasonable match to the composite spectrum derived from observations and also produces roughly the same luminosity at high energies as the bremsstrahlung spectrum. However, the ionizing luminosity in our model is much higher than that in the PK04 simulation, since we allow both disk and central source photons to contribute to the ionizing flux. We return to this point in Section 4.1, where we explicitly check the impact of this difference on the calculated ionization state of the wind. Our adopted parameters are summarised in Table 1.

3. RESULTS

Parameter	Value
M_{BH}	$10^8 M_\odot$
\dot{M}_{acc}	$1.8 M_\odot yr^{-1} \approx 0.5 \dot{M}_{Edd}$
Γ_X	2.1
$L_{2-10 eV}$	2.7×10^{44} ergs s^{-1}
$r_{disk(min)} = r_X$	$6R_G = 8.8 \times 10^{13}$ cm
$r_{disk(max)}$	$2700R_G = 4 \times 10^{16}$ cm

Table 1

The key parameters adopted in the radiative transfer simulation.

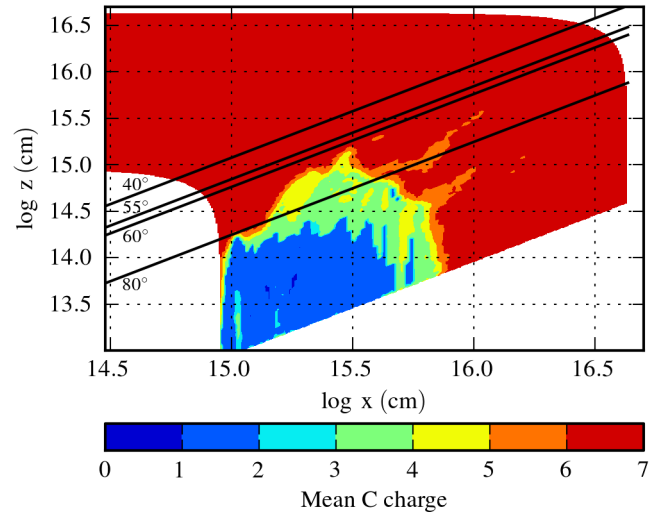


Figure 4. The mean charge of carbon in the model.

We are now ready to present the key properties of our converged wind model. We will first illustrate the ionization state of the wind and then present the simulated emergent spectra. Finally, we will also show the temperature structure and ionization parameter throughout the outflow.

3.1. Ionization state

We begin by considering the ionization state of carbon, since strong, blueshifted absorption associated with C iv 1550 Å is a defining feature in the UV spectra of essentially all BALQSOs. However, as illustrated in Figure 4, carbon is actually fully ionized throughout much of the outflow. In the very dense ‘failed wind’ at the base of the wind, carbon is in a much lower ionization state. This is partly due to the high density in this region, but also to photoelectric absorption in the outer skin of the wind, which removes a large proportion of the soft X-ray photons responsible for ionizing carbon. In PK04, the warm outflow behind the failed wind also remained in a low ionization state. However, in our calculation, the carbon in this area is fully ionized. This key difference is due to scattered and reprocessed radiation and is discussed in more detail in section 4. Figure 4 also illustrates the sight-lines for which we produce synthetic spectra.

Figure 5 shows the mean charge of iron in the model and can be directly compared to Figure 3 in SP10. The computed ionization states are very similar. This shows that the inclusion of an accretion disk in our simulation as a source of ionizing photons has not altered the conclusions of the earlier work with regards to species whose ionization state is mainly set by the incident X-ray flux.

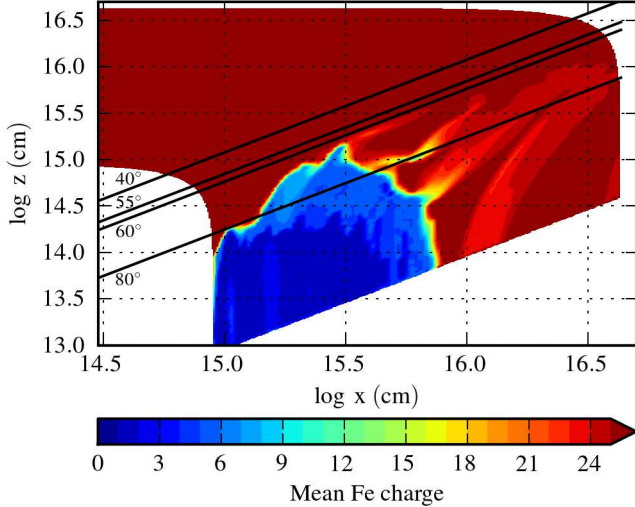


Figure 5. The mean charge of iron in the model (c.f. Sim et al. 2010).

3.2. Synthetic spectra

Figure 6 shows synthetic spectra computed for the four sightlines illustrated in Figure 4. For comparison, the spectrum that would be seen in the absence of any absorbing material (labelled “unabsorbed”) is also shown as a faint grey line for each sightline. The 80° sightline passes through the failed wind region where carbon is not fully ionized. This is the most likely place to look for absorption from moderately ionized species. However, the simulated spectrum for this sightline (the heavy black line) is almost entirely featureless except for a small absorption feature at 255 Å due to a resonance line of Fe xxiv. The other three spectra in this plot show the proportion of the net spectrum made up from unscattered, singly scattered and multiply scattered photons. These contributions reveal why we do not see any absorption features associated with the species present in the failed wind: essentially all of the photons escaping along this direction have scattered at least once and about 50% of them have scattered more than once. Thus the net spectrum for this sightline is produced by photons that have scattered *around* the failed wind, rather than passing through it. Fe xxiv is present in the equatorial, outflowing wind behind the failed wind region (see Figure 5) and scattered photons pass through regions of the wind where this ion is present. The direct (unscattered) component of the radiation field escaping along this sightline is very heavily attenuated by a combination of photoionization absorption and electron scattering.

The 60° sightline skims the top of the failed wind. Here, the component of the synthetic spectrum associated with photons that did not undergo any scattering events is only slightly less than 50% of the total. As the viewing angle moves even further up, to 55°, most of the photons escape unscattered. The Fe xxiv feature is still present at 60°, but only in the direct component. The spectrum predicted for the 55° sightline is completely featureless.

The final spectrum is computed for a sightline of 40°, and here we see a continuum enhancement at wavelengths below about 700 Å. This is a consequence of the geometry of the wind model: photon packets with wavelength less than 700 Å are predominantly produced by parts of the accretion disk in-

wards of the innermost radial extent of the wind (60 R_G). The spectrum is therefore made up of a direct component of photons passing unimpeded from the disk into the relatively low density polar parts of the wind (direct component), and photons reflecting from the inner face of the failed wind (scattered component). By contrast, a significant proportion of photon packets with wavelength longer than 700 Å are produced from parts of the accretion disk under the dense failed wind, and this component will tend to be absorbed or scattered back into the disk. We therefore only see a fraction of the direct component. Even when supplemented by scattered radiation, the resulting flux is less than would be seen in the wind were not present at all. The continuum enhancement at low inclination angles was also predicted in the X-ray spectra computed in SP10, where it was also attributed to reflection from the innermost illuminated face of the ‘failed wind’ region.

3.3. Temperature distribution

The top two panels of Figure 7 show the electron temperature T_e computed for the hydrodynamic model on two different scales. The left hand matches the scale of the two lower plots, while the right hand panel is optimised to show the full range of temperatures obtained in the current calculations. The lower left panel shows the temperature structure estimated by PK04, whilst the lower right hand panel shows the temperature structure found by SP10. The clearest difference between the temperature computed in the hydrodynamic simulation and that found here is in the low density in-falling flow towards the polar direction. In this region, Compton heating and cooling are the dominant mechanisms, and so the temperature depends on the mean frequency of photons in the region. Since we include the radiation field produced by the accretion disk in our ionization and thermal equilibrium calculations of ionization, the mean frequency we find is far lower than that assumed in PK04, where only the 10 keV Bremsstrahlung spectrum was used to compute the ionization state and temperature structure. The temperature structure found by SP10 is closer to ours, since they also included an assumed disk spectrum in their calculation of Compton cooling. In any case, the exact temperature in this polar region is actually not all that important, since the density there is far too low to imprint any spectral features.

Another interesting difference is seen in the transition zone, where the PK04 calculation contains very hot ‘streamers’ of shock-heated gas. We do not model this non-radiative heating mechanism, and so our wind does show these structures. Again, this difference does not affect the simulated spectra or our wider conclusions, since this region is fully ionized in both cases.

Finally, a much more important difference is in the warm equatorial flow. This region lies behind the dense ‘failed wind’ region which is very cold all three calculations. In PK04, the ionization parameter was used to calculate the temperature in the model. This, in turn, was calculated using the X-ray luminosity of the central source, attenuated by electron scattering opacity and distance. In the dense equatorial flow, this estimate of the ionization parameter is very low, and the treatment used in PK04 (described in detail in Proga, Stone & Kallman 2000) yields unrealistically low temperatures. In such cases, they assumed that the gas would be in local thermodynamic equilibrium, and the temperature was set to be equal to the temperature of the disk below it. However, our more detailed radiative transfer treatment per-

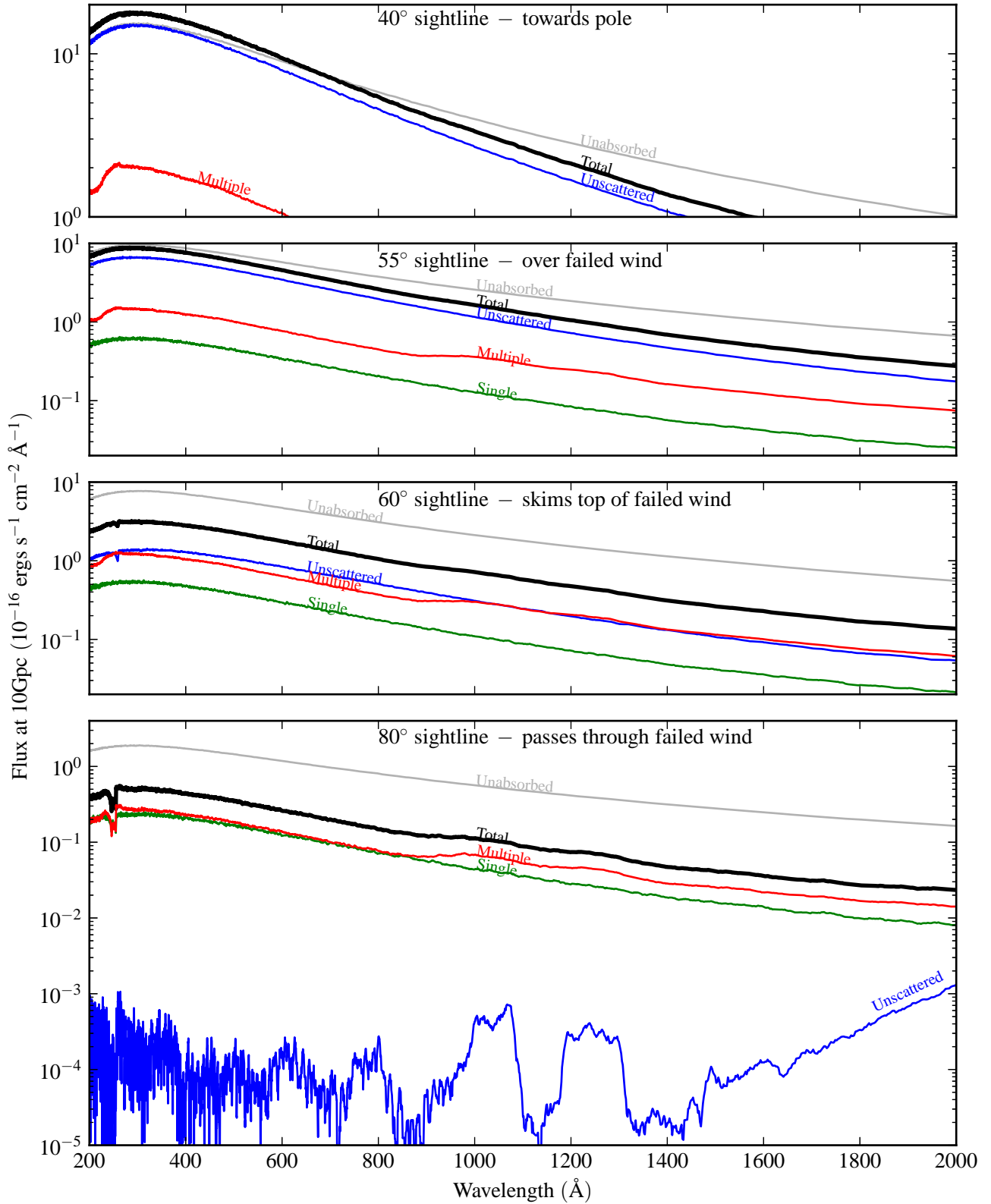


Figure 6. The simulated spectrum for three sightlines. The grey line is the flux that would be observed if there were no wind present. The heavy line shows the simulated spectrum for the converged wind model, and the remaining three lines split that spectrum into components. The blue line shows the part of the escaping flux associated with photons that have not scattered in the model, the green line shows the part associated with photons that have scattered just once, and the red line shows the part associated with multiply scattered photons.

mits photons to scatter around the failed wind, and these scattered photons turn out to be the dominant source of ionization and heating in the equatorial flow region. We therefore obtain temperatures of a few hundred thousand Kelvin for this region, significantly hotter than in PK04, but similar to the temperatures obtained by SP10, whose calculation also allowed for scattering. We discuss the critical consequences of this finding in Section 4.

3.4. Ionization parameter

In Figure 8, we show the ionization parameter U , computed for each cell in the model based on the actual photon packets that have passed through the cell. The standard definition of U is

$$U = \frac{Q(H)}{4\pi r_0^2 n(H)c}, \quad (1)$$

where $Q(H)$ is the number of photons emitted by the source per second, r_0 is the distance from the illuminated cloud to the source, and $n(H)$ is the number density of hydrogen. Thus U is simply the ratio of the number density of ionizing photons, $n(\gamma_H)$, to the number density of hydrogen atoms. We explicitly track this information in our simulation, and so our version of U for each cell is given by

$$U = \frac{n(\gamma_H)}{n(H)}. \quad (2)$$

In the optically thin case, both definitions will give identical values of U . However, our version self-consistently takes account of any absorption between the source and the cell, along with additional photons which may scatter into the cell from other lines of sight.

Figure 8 shows immediately why we do not have any C IV in the wind. In order for a significant fraction of Carbon ions to be found in this ionization stage, we require $\log(U) \sim -2$ (Higginbottom et al. 2013). There are no parts of the wind where this is true. There are also significant implications of this ionization parameter distribution on the self-consistency of the hydrodynamic model, since efficient line driving is only possible for significantly lower values of ionization parameter than we predict for the outflowing parts of the simulation. We discuss this further below.

4. DISCUSSION

We are now in a position to consider some key aspects and consequences of our results in more detail. First, we will attempt to isolate the cause of the discrepancy between the temperature structure and ionization state found by PK04 and those calculated above. Second, we will look at the way in which photons actually propagate through the PK04 model in order to address what the structure of a viable line-driven disk wind might be. Third and finally, we will discuss the implications of our study for dynamical simulations of line-driven winds.

4.1. Why is the wind hotter and more ionized than predicted by PK04?

There are several key differences between the calculation of the temperature and ionization state of the wind in PK04 and that described above:

- Input spectrum: PK04 used a 10 keV Bremsstrahlung spectrum to compute both the ionization parameter and the temperature of the wind; by contrast, we have used

an observationally motivated AGN spectrum that includes ionizing radiation associated with both the accretion and a central X-ray source.

- Wind radiation: in our model, photons produced by the wind itself are able to interact with (e.g. ionize) other parts of the outflow; in PK04, the wind was assumed to be transparent to its own cooling radiation.
- Scattering: in PK04, the local radiation field at each point in the wind was assumed to be dominated by *direct* radiation from the central engine, with electron scattering treated as a purely absorptive process; here we take full account of all opacity mechanisms and in particular we track the propagation of scattered photons through the flow.

To assess the relative importance of these effects, Figure 9 shows the distribution of the ionization parameter throughout for two additional test cases. The ionisation parameter is a useful parameter to compare here, since it largely defines the ionization state of the wind and is also used to compute the temperature and line-driving force in PK04.

The upper right panel in Figure 9 shows the ionization parameter as presented in Figure 1 in PK04. However, we have converted the definition of the ionization parameter adopted in PK04 (ξ) to that adopted here (U), using their approximate formula $\log(U) = \log(\xi) - 1.75$. Comparing this to Figure 8, we immediately see that our values of U are consistently higher than those found by PK04.

To test how much of this difference is due simply to the differences between the adopted illuminating spectra, we have rerun our simulation, with the accretion disk removed as a radiation source and with the X-ray spectrum modified to a power-law that approximates the 10 keV Bremsstrahlung spectrum assumed in PK04, i.e. $F_\nu \propto \nu^0$. This X-ray spectrum is normalized so as to give the same luminosity over the 2–10 keV range as the PK04 SED, and the high-frequency cutoff of the Bremsstrahlung spectrum is approximated by truncating the power law at 10 keV. This input spectrum is used for all three of the new calculations shown in Figure 9.

The ionization parameter calculated for the wind in the absence of a disk radiation field is shown in the upper left panel of Figure 9. Based on this, we can conclude that the difference between the ionizing SED adopted by us and in PK04 is the main reason for the discrepancy between the estimates of U in the polar wind regions. This is unsurprising since the wind is optically thin in these directions. However, the critical region for the viability line-driving and the production of broad UV absorption lines is the warm, equatorial outflow. Here, U is uniformly very small in the PK04 data, but remains at $\log(U) \gtrsim 2$ outside the dense failed wind region even in our simulation without disk photons. This ionization parameter is too high to support line driving (Stevens & Kallman 1990).

In the lower left panel of Figure 9, we show U from the same no-disk calculation, but taking into account only photons that have not undergone any scattering events, i.e. only photons arriving directly from the central source or emitted by the wind. We now see a moderate decrease in U throughout the whole model except the bulk of the failed wind. This is consistent with the failed wind efficiently scattering photons into the polar regions in our standard calculation, and with regions shielded by the failed wind being affected strongly by radiation scattered around the shield. However, the ioniza-

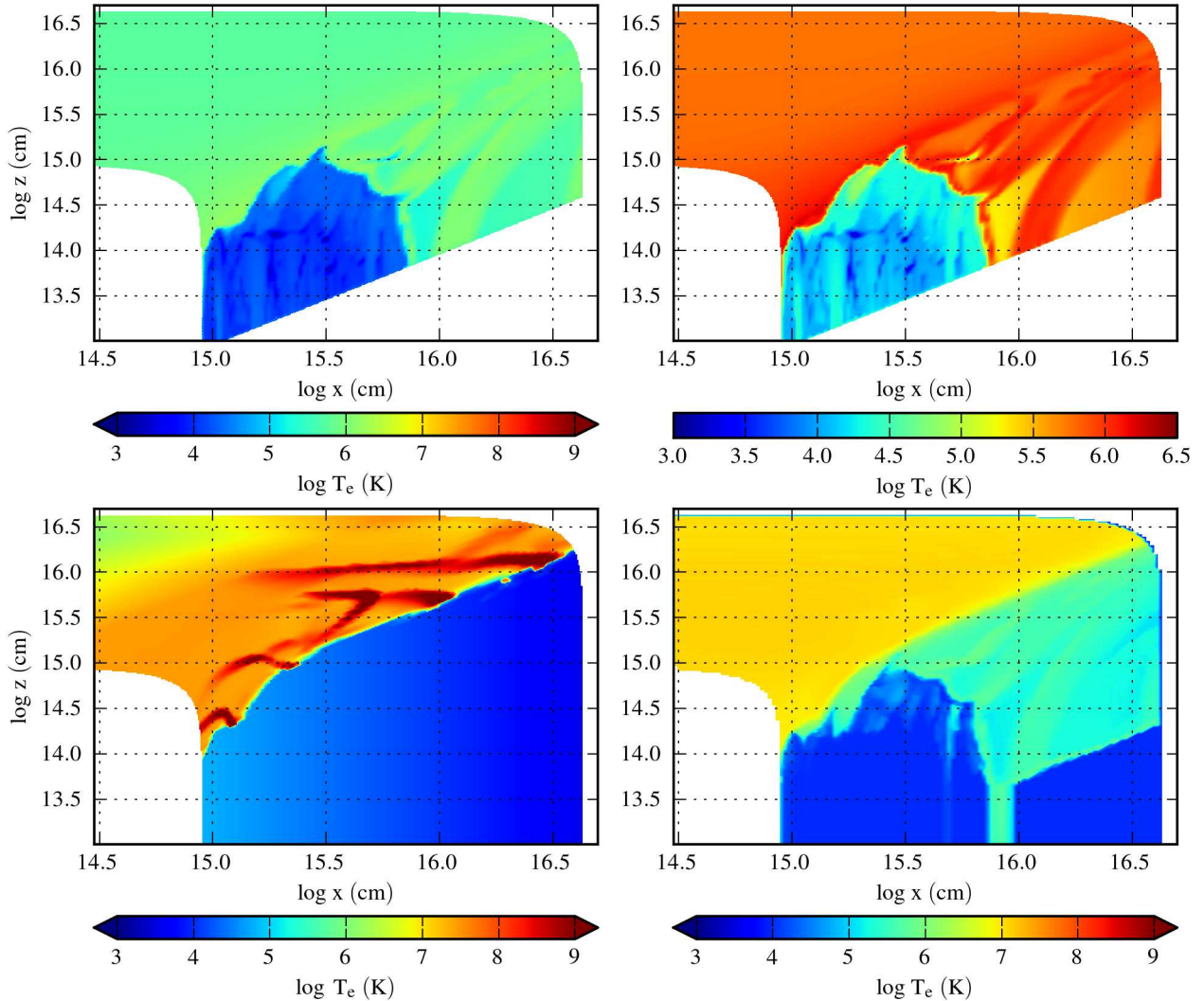


Figure 7. The electron temperature (T_e) of the model calculated here, compared to that from PK04 and SP10. The top two panels show the current calculation, but on different colour scales. The upper right scale is optimised for the data, whilst the top left is on an identical scale to the lower two plots. The lower left panel is the temperature from the original PK04 calculation, whilst the lower right panel shows the temperature from SP10.

tion parameter in the warm, equatorial outflow region is still higher than in PK04 and still too high for efficient line driving.

Finally, in PK04, the wind is able to cool via radiative processes, but is assumed to be optically thin to its own radiation. We therefore carry out another no-disk, unscattered-photons-only calculation, but now also disable wind emission in the `PYTHON` simulation. More specifically, the wind is still allowed to cool via radiative processes, but no photons are produced that could interact with other parts of the wind. The result is shown in the lower right panel of Figure 9. Only in this last calculation, which most closely mimics the approximations made in PK04, does $\log(U)$ drop to a level where line driving could become efficient.

4.2. The propagation of ionizing photons through the outflow: implications for line-driving

We have seen that taking account of wind emission, multiple scattering and including the accretion disk as a source of ionizing radiation has resulted in an outflow that is too highly

ionized for line driving to work efficiently as an acceleration mechanism. However, this does not mean that line driving could not produce an outflow at all. If one were to compute a new step in the hydrodynamical calculation based on our new ionization state, the line-driving forces, and hence the outflow structure, would certainly change (relative to the same time step in PK04's original simulation). The key question is whether the end result would be a total quenching of the wind or whether the flow might adjust itself to a new configuration in which line driving can be effective again. A self-consistent 3-dimensional radiation-hydrodynamic calculation would be needed to answer this question definitively, and we briefly comment on the prospects for this in Section 4.3 below. However, by considering the way in which ionizing radiation actually propagates through the outflow, we can already comment on the general properties of any viable line-driven disk wind model.

In Figure 10, we show some characteristics of the ionizing photons that reach three particular cells in the wind. One

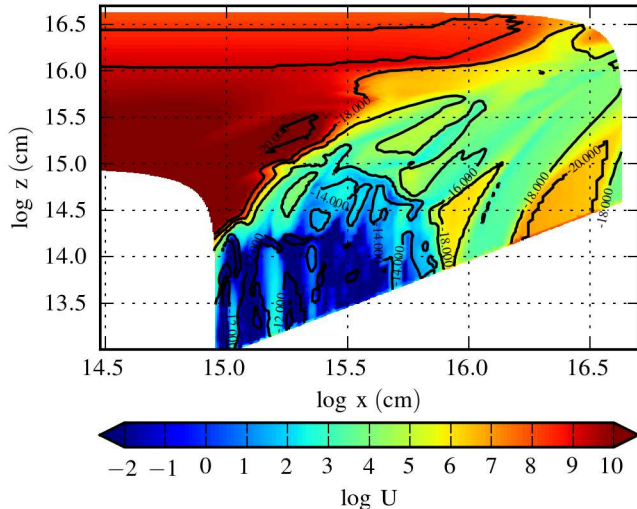


Figure 8. The ionization parameter $\log(U)$ in each cell of the model. The contours show the underlying density of the model.

cell (1 - marked with the triangle in the upper panel) is in the highly ionized, low density part of the model and serves as a comparison to the other two cells (2 - marked with a circle, and 3 - marked with a square), both of which are in the outflowing part of the model. In PK04, cells 2 & 3 are characterized by the relatively low ionization states required for efficient line driving. In our calculations, these cells are highly ionized, so that line driving could not be effective in them. Also shown in the upper panel are the starting locations of the ionizing photons emitted by the wind that pass through cell 2. Broadly speaking, these photons turn out to originate in the outside skin of the failed wind. This region sees and absorbs a significant fraction of the ionizing radiation generated by the disk and the X-ray source. Since the wind is assumed to be in radiative and thermal equilibrium, all of this absorbed energy must be locally re-emitted.

The middle panel in Figure 10 shows the distribution of the initial launch radii of the ionizing disk photons that pass through our test cells. The detached symbols near the left-hand-side of the plot show the corresponding fraction of photons emitted by the central X-ray source for comparison. We can see immediately that, for all cells, the majority of ionizing photons arise in the inner parts of the accretion disk. In PK04, the region above this part of the disk was outside the computational domain, and so it is empty in our calculation as well. Photons generated in this part of the disk are therefore able to reach the wind without attenuation. In the hydrodynamic calculation, this was done for reasons of computational efficiency, but it is also physically reasonable, since the temperature and ionization state of the gas above this part of the disk would likely be too high to permit efficient line driving. Nonetheless, the additional failed wind region that would likely result if this region was included in the simulation would certainly modify the spectrum incident on the rest of the wind and might result in a lower ionization state there. Extending the computational domain down to the innermost parts of the disk would therefore be an important next step in understanding line-driven winds. Useful steps towards this have already been taken in radiation-(magneto)hydrodynamic simulations of accretion disks (e.g.

Ohsuga & Mineshige 2011; Jiang, Stone & Davis 2013).

The middle panel of Figure 10 also shows that the launch radius distribution of ionizing photons is similar for all three test cells, even though two of the cells (nos. 2 and 3) are located in the shadow of the failed wind region, as seen from the central engine. Thus the failed wind does not provide an effective shield from ionizing radiation. As already shown in Figure 6 and discussed in Section 3, this is because scattering allows photons to reach parts of the flow that would otherwise be shadowed. Interestingly, the radiation field in cells 2 and 3 also includes some photons generated in the outer parts of the disk; for example, about 10% of the ionizing photons reaching cell 3 come directly from the disk beneath it. This is possible because the outflow density and opacity has dropped significantly at these larger radii.

Finally, the lower panel of Figure 10 shows the distribution of launch angles (relative to the vertical axis) for all ionizing photon packets produced by the disk and central X-ray source that ultimately pass through the three test cells. The direct sightline from the origin to cell 1 corresponds to an angle of 26.5° , and the launch angle of most photons that reach this cell is, in fact, close to this value. However, a significant fraction of the ionizing photons in this cell were originally emitted in a more equatorial direction and only reach the cell after scattering off the failed wind. These photons produce the hump near 65° in the photon launch angle distribution for cell 1. Cells 2 and 3 (which lie at a sightline from the origin of 80°) are shielded from the direct radiation produced by the central X-ray source and inner disk by the failed wind. The ionizing photons reaching these cells instead exhibit a wide distribution of initial launching angles, peaking around 58° . This direction is marked by the lower straight line in the top panel of Figure 10. Photons taking this initial path interact with the hot transition region of the flow, i.e. the upper skin of the failed wind. When they enter this region, the optical depth along their trajectory is much higher than that perpendicular to it, so they are preferentially scattered both up into the polar regions and down into the parts of the flow behind the failed wind. Photons with initially more equatorial directions will initially strike the failed wind region. A significant fraction of these photons will be reflected back across the inner disk and enter the transition region on the other side of the grid. Some of these photons will then once again be scattered in the outflow region behind the failed wind.

This analysis suggests that it is the transition region (i.e. region B in Figures 1 and 2) that is mainly responsible for redirecting ionizing photons into the outflow regions behind the failed wind. This applies not only to photons emitted by the central X-ray source and inner disk, but also to photons produced by the “front” of the wind itself. Thus, even though *the failed wind is doing its job in preventing direct illumination* from reaching the outflow behind it, ionizing photons can get around it via scattering in the transition region.

How might we expect the outflow to respond? Given the over-ionization of the outflow behind the failed wind, it seems likely that the outflow in this region would also fail. This would result in a larger failed wind region - perhaps reducing the ionization state of the material behind this extended block. However, since the failed wind is already highly optically thick in the radial direction, and since scattered and reprocessed radiation is already dominant in the shielded region, this effect is likely to be quite small.

Given the importance of the transition region in redirecting ionizing photons into otherwise shielded parts of the flow, it

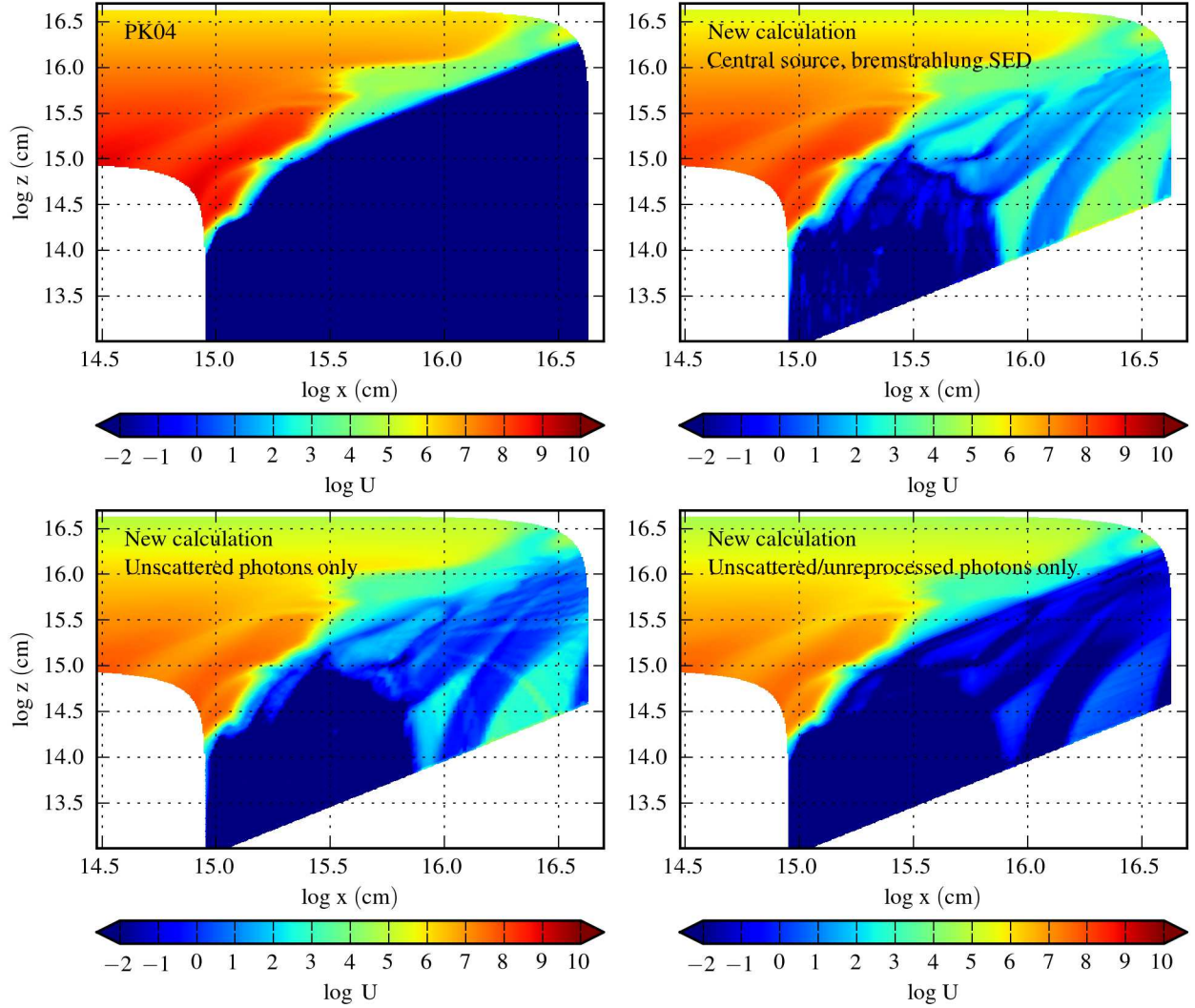


Figure 9. The upper left panel shows the ionization parameter from PK04 (scaled from their definition ξ to ours via $\log(U) = \log(\xi) - 1.75$). The remaining three panels all show results from `rython` calculations that use an approximation to the 10 keV bremsstrahlung spectrum assumed in PK04 as the only source of photons. The upper right panel shows U calculated taking into account all photons in the cell, whilst the lower panel only counts photons arriving directly from the X-ray source (i.e. unscattered photons). The lower right panel shows U from a calculation where the wind is permitted to cool via radiative processes, but the resulting photons are not actually produced and tracked in the simulation. This is analogous to the approximation made in PK04. Here, again, only unscattered photons used to calculate U (i.e. only unscattered and unreprocessed photons).

seems likely that it is this region that would have to be modified to allow the formation of a line-driven outflow. In the PK04 model, the geometry of this transition region allows photons that would otherwise pass over the outflow to be efficiently scattered down into it. If this transition region instead had a more curved upper surface profile, photons missing the failed wind could not be scattered so easily back down into the outflow behind this region. Is it plausible that the flow might adjust itself to form such a geometry? Possibly. In the PK04 model, line driving already only just works in the transition region, since the ionization state there is fairly high. Given the even higher ionization state we predict for this region, line driving would likely fail completely, causing the material to drop back to the disk, perhaps forming the geometry required to produce an effective shield. However, fully self-consistent calculations would be required to test this idea.

4.3. Implications for hydrodynamic simulations of line-driven winds

The analysis we have carried out on the PK04 geometry has clearly shown that reprocessing and scattering effects have a significant – and actually dominant – effect on the ionization state of the wind. This, in turn, must strongly affect the efficiency of the line driving mechanism itself. The clear conclusion from our results is therefore that these radiative effects must somehow be incorporated into hydrodynamic simulations.

The most obvious way to achieve this would be to carry out a full radiative transfer and ionization calculations after each time step of the hydrodynamic simulation. However, the main radiative transfer calculation presented here takes about 10 hours of processing time on 192 processors of the Southampton University Iridis supercomputer. Thus, even if

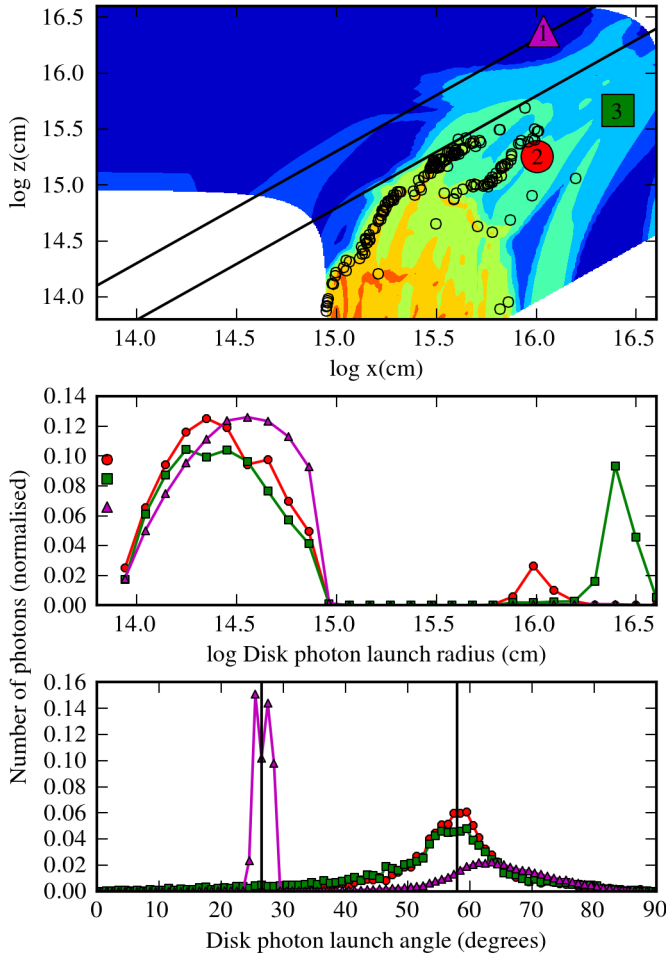


Figure 10. Illustration of the source of ionizing photons contributing to the radiation field in three cells. The top panel shows the location of the three cells (filled symbols), along with the starting locations of wind generated photons that reach cell 2 (open circles). The underlying colours show the density of the model - note that the colour scale here is different to that used in Figure 2. The two straight lines in this plot correspond to two specific sightlines: the top line marks $i \approx 26.5^\circ$, the sightline passing from the origin through cell 1; the bottom line marks $i \approx 58^\circ$, a sightline passing through the transition region between the failed wind and the polar regions of the outflow. The middle panel shows the launch radius of the disk generated photons that reach the three cells (plot symbols match the symbols used to mark each cell in the top panel). The proportion of photons originating from the central X-ray source is also shown via the isolated symbols near the left hand side of the plot. The bottom panel shows the initial launch angle (relative to the vertical axis) of the same photons. The vertical lines mark the two angles also shown as sightlines in the top panel. In the lower two plots, the ordinate is normalised to the total number of photons reaching the cell in question.

such a scheme could be implemented, it is not at all clear that it is computationally feasible at this time. Nonetheless, it is important to develop at least an approximate method along these lines in order to obtain robust results from line-driven wind simulations.

It should be noted that it is not only full hydrodynamic simulations of line-driven winds that have treated radiative transfer in a simplified manner. Calculations such as those presented in Risaliti & Elvis (2010) and Nomura et al. (2013) also neglect scattered and reprocessed radiation and give rise to wind solutions similar to that presented in PK04. It is therefore likely that similar effects would be seen in these models.

5. CONCLUSIONS

We have presented results from comprehensive radiative transfer and photoionization calculations for the line-driven AGN disk wind predicted by the hydrodynamic simulations carried out in PK04. These simulations were computationally expensive and therefore treated the radiative transfer and ionization in a simplified manner. Here, we have focused on one snapshot from the hydrodynamic calculation and carried out a much more detailed Monte-Carlo simulation of the interaction between the AGN radiation field and the outflow.

Our main result is that the ionization state of the outflow is much higher than estimated by PK04, to the extent that line-driving would become inefficient. The over-ionized flow also no longer produces the broad UV absorption lines that are the key observational tracers of disk winds in AGN/QSOs. The main reason for this change in the predicted ionization state of the flow is that self-shielding becomes much less effective when radiative transfer effects are fully accounted for. More specifically, the failed wind region that protects the outflow from over-ionization in the simulations of PK04 can actually be ‘‘circumnavigated’’ by ionizing photons via scattering and reprocessing.

We conclude that hydrodynamic disk wind simulations need to take account of scattering and reprocessing in order to robustly assess the viability of line driving as an acceleration mechanism. This should ideally take the form of a self-consistent treatment, in which the radiative transfer and hydrodynamics are calculated simultaneously. However, the kind of ‘post-processing’ approach we have used here is at least useful in validating purely hydrodynamic models. For outflows driven non-radiatively, it already provides a means to self-consistently predict the observational characteristics of the flow.

ACKNOWLEDGEMENTS

The work of NH, JHM and CK are supported by the Science and Technology Facilities Council (STFC), via studentships and a consolidated grant, respectively. DP acknowledges Support for Program number HST-AR-12150.01-A that was provided by NASA through a grant from the Space Telescope Science Institute, which is operated by the Association of Universities for Research in Astronomy, Incorporated, under NASA contract NAS5-26555. This work was also supported by NASA under Astrophysics Theory Program grants NNX11AI96G.

REFERENCES

- Arav, N., Korista, K. T., Barlow, T. A. & Begelman, 1995, *Nature*, 376, 576
- Arav, N. 1996, *ApJ*, 465, 617
- Begelman, M. C., McKee, C. F. & Shields, G. A. 1983, *ApJ*, 271, 70
- Begelman, M., de Kool, M. & Sikora, M. 1991, *ApJ*, 382, 416
- Blandford, R. D. & Payne, D. G. 1982, *MNRAS*, 199, 883
- Cottis, C. E., Goad, M. R., Knigge, C. & Scaringi, S. 2010, *MNRAS*, 406, 2094
- Davis, S. W. & Laor, A. 2011, *ApJ*, 728, 98
- Done, C., Davis, S. W., Jin, C., Blaes, O. & Ward, M. 2012, *MNRAS*, 420, 1848
- Higginbottom, N., Knigge, C., Long K. S., Sim, S. A., & Matthews J. H. 2013, *MNRAS*, 436, 1390
- Jiang, Y. F., Stone, J. M. & Davis, S. W. 2013, *ApJ*, 778, 65
- Kallman, T. R. & McCray, R. 1982, *ApJS*, 50, 263
- Kashi, A., Proga, D., Nagamine, K., Greene, J. & Barth, A. J. 2013, *ApJ*, 778, 50
- Knigge, C., Scaringi, S., Goad, M.R. & Cottis, C.E. 2008, *MNRAS*, 386, 321
- Krolik, J. H. & Kriss, G. A. 2001, *ApJ*, 561, 684

- Laor, A., Fiore, F., Elvis, M., Wilkes, B. J., & McDowell, J. C. 1997, *ApJ*, 477, 93
- Long, K. S. & Knigge, C. 2002 *ApJ*, 579, 725L
- Lusso, E., Comastri, A., Simmons, B. D., Mignoli, M., Zamorani, G., Vignali, C., Brusa, M., Shankar, F., Lutz, D., Trump, J. R., Maiolino, R., Gilli, R., Bolzonella, M., Puccetti, S., Salvato, M., Impey, C. D., Civano, F., Elvis, M., Mainieri, V., Silverman, J. D., Koekemoer, A. M., Bongiorno, A., Merloni, A., Berta, S., Le Floch, E., Magnelli, B., Pozzi, F. & Riguccini, L. 2012, *MNRAS*, 425, 623.
- Murray, N., Chiang, J., Grossman, S. A. & Voit, G. M. 1995, *ApJ*, 451, 498
- Nomura, M., Ohsuga, K., Wada, K., Susa, H. & Misawa, T. 2013, *PASJ*, 65,40
- North, M., Knigge, C. & Goad, M. 2006, *MNRAS*, 365, 1057
- Ohsuga, K. & Mineshige, S. 2011, *ApJ*, 736, 2
- Pelletier, G. & Pudritz, R. E. 1992, *ApJ*, 394, 117
- Proga, D., Stone, J. M. & Kallman, T. R. 2000, *ApJ*, 543, 686
- Proga, D. & Kallman, T. R. 2004, *ApJ*, 616, 688P
- Proga, D., & Kurosawa, R. 2010, *ASPC*, 427, 41
- Elvis, M. & Risaliti, G. 2010 *A&A*, 516A, 89R
- Schurch, N. J., Done, C. & Proga, D. 2009, *ApJ*, 694, 1
- Shakura, N. I. & Sunyaev, R. A. 1973, *A&A*, 24, 337
- Shlosman, I., Vitello, P. A. & Shaviv, G. 1985. *ApJ*, 294, 96
- Sim, S. A., Proga, D., Miller, L., Long, K. S. & Turner, T. J. 2010, *MNRAS*, 408, 1396
- Slone, O. & Netzer, H. 2012, *MNRAS*, 426, 656
- Stevens, I. R. & Kallman, T. R. 1990, *ApJ*, 365, 321
- Stone, J. M. & Norman, M. L. 1992, *ApJS*, 80,753
- Weymann, R. J., Scott, J. S., Schiano, A. V. R. & Christiansen, W. A. 1982, *ApJ*, 262, 497
- Zheng, W., Kriss, G. A., Telfer, R. C., Grimes, J. P. & Davidsen, A. F. 1997, *ApJ*, 475, 469